

QED-driven laser absorption

M. C. Levy,^{1,*} T. G. Blackburn,² N. Ratan,¹ J. Sadler,¹ C. P. Ridgers,³ M. Kasim,¹ L. Ceurvorst,¹ J. Holloway,¹ M. G. Baring,⁴ A. R. Bell,¹ S. H. Glenzer,⁵ G. Gregori,¹ A. Ilderton,^{2,6} M. Marklund,² M. Tabak,⁷ and S. C. Wilks⁷

¹*Department of Physics, University of Oxford, Parks Road, Oxford OX1 3PU, UK*

²*Department of Physics, Chalmers University of Technology, SE-41296 Gothenburg, Sweden*

³*York Plasma Institute, University of York, York, YO10 5DD, UK*

⁴*Department of Physics and Astronomy, Rice University, Houston, Texas 77005, USA*

⁵*SLAC National Accelerator Laboratory, 2575 Sand Hill Road, Menlo Park, CA 94025*

⁶*Centre for Mathematical Sciences, Plymouth University, PL4 8AA, UK*

⁷*Lawrence Livermore National Laboratory, Livermore, California 94551, USA*

(Dated: August 8, 2019)

Absorption covers the physical processes which convert intense photon flux into energetic particles when a high-power laser illuminates optically-thick matter. It underpins important petawatt-scale applications today, *e.g.*, medical-quality proton beam production. However, development of ultra-high-field applications has been hindered since no study so far has described absorption throughout the entire transition from the classical to the quantum electrodynamical (QED) regime of plasma physics. Here we present a model of absorption that holds over an unprecedented six orders-of-magnitude in optical intensity and lays the groundwork for QED applications of laser-driven particle beams. We demonstrate 58% efficient γ -ray production at 1.8×10^{25} W cm⁻² and the creation of an anti-matter source achieving 4×10^{24} positrons cm⁻³, $10^6 \times$ denser than of any known photonic scheme. These results will find applications in scaled laboratory probes of black hole and pulsar winds, γ -ray radiography for materials science and homeland security, and fundamental nuclear physics.

CONTENTS

I. Introduction	1
II. Absorption Model	3
A. Classical Relativistic Absorption	3
B. Strong-Field QED Processes	3
1. Quantum γ -ray Radiation	4
2. Electron-Positron Pair Production	5
C. Feedback Between QED and Classical Dynamics	6
III. Comparison to QED-PIC Simulation Results	7
IV. Conclusion	8
A. QED-PIC Simulations	8
References	9

I. INTRODUCTION

The peak focal intensities produced by high-power laser technology have undergone rapid increases since the advent of chirped-pulse amplification in the late 1980s [1]. Today, the record intensity has reached up to 10^{22} W cm⁻² and next-generation facilities such as the Extreme Light Infrastructure (ELI) will achieve in excess of 10^{24} W cm⁻² at optical wavelengths [2]. These lasers

have the potential to shed light on the structure of the quantum vacuum [3, 4], settle an ultimate upper limit to the attainable intensity of an electromagnetic wave [5–7], discern the transition between classical and quantum radiation reaction [4, 8, 9], and provide efficient sources of intense γ -rays and dense anti-matter [10, 11]. However, all analyses of optically-thick QED plasma thus far have been restricted to numerical studies [11–13] and simplified situations where the ion mass is infinitely-large [14], the laser polarization is such that the fast-oscillating component of the nonlinear heating force vanishes, or γ -ray radiation is treated in a classical fashion [15–17].

By combining strong-field QED with recent advances in plasma kinematic theory [18, 19], we present the first analytical absorption model which elucidates how optically-thick matter responds to high-power laser illumination from the scale of today’s petawatt lasers all the way to the QED electron-positron pair cascade. To span these optical laser intensities this work, for the first time, self-consistently accounts for quantum mechanically-correct γ -ray emission, hydrodynamic particle injection, and e^-/e^+ field-screening taking place in the partial standing wave set up by laser absorption.

Key features of the model are depicted schematically in Fig. 1 (a). Here a thick slab of opaque matter is illuminated at normal incidence by a linearly-polarized high-power laser beam having peak dimensionless strength parameter $a_0 = eE/mc\omega$, where E is the laser electric field and ω is its angular frequency. Over the Lorentz-transformed collisionless skin depth λ_p shown in dark red, the laser rapidly field-ionizes the matter to create a supercritical plasma, *i.e.*, with electron density n_0 exceeding the relativistically-correct critical density $a_0 n_c$ where

* matthew.levy@physics.ox.ac.uk

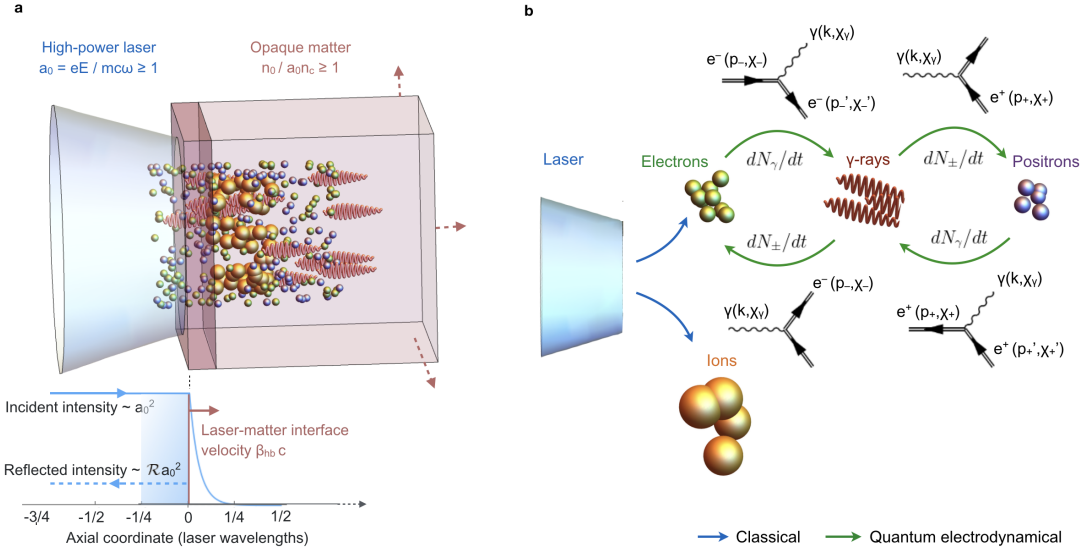


FIG. 1. **The response of optically thick matter to high-power laser light.** (a) Relativistic particle flows are produced through absorption when a high-power laser is shined onto optically-thick matter. Along the laser-matter interface ultrafast field-ionization creates a thin layer of opaque plasma. (b) The electrons and ions are accelerated via classical electromagnetic absorption processes [19, 20]. Leptons are cooled through the emission of quantum synchrotron γ -ray photons in the ultra-strong optical field. The γ -rays “decay” into electron-positron pairs which become electromagnetically accelerated, thereby linking together the classical and quantum electrodynamical absorption. Thick double-lines in the Feynman diagrams indicate “dressed” charged-particle states which account to all orders in a_0 for the effect of the classical laser field.

$n_c = \varepsilon_0 m \omega^2 / e^2$ (ε_0 is the vacuum permittivity). We use $1\mu\text{m}$ wavelength light and a model geometry centered at the supercritical interface determined by $n_0/a_0 n_c \simeq 1$ so that the laser evanescences over λ_p in the downstream matter. n_0 is thusly scaled linearly with a_0 to maintain the optically-thick condition, which in the classical regime introduces a similarity to the electron dynamics [21].

The interface itself is accelerated to an appreciable fraction of light-speed β_{hb} along the wave propagation vector by pressure associated with the intense photon flux. This “hole-boring” electrostatic process accelerates ions to moderately-relativistic energies and reduces through hydrodynamic motion the optical photon flux deposited onto the interface [18]. In the upstream vacuum region, indicated using blue shading, collisionless classical and QED absorption processes create γ -rays and e^- and accelerate highly-relativistic e^-/e^+ through the interface into the dense matter bulk.

The relevant interactions are therefore highly localized (we show that the axial lengthscale is smaller than λ) and the instantaneous fractional absorption into each particle species is equivalent to [18, 19],

$$f_k = \frac{1}{1 - \beta_{hb}} \frac{v_k}{c} \frac{n_k}{u_1} \langle \mathcal{E}_k \rangle, \quad f = \sum_k f_k = 1 - \mathcal{R}, \quad (1)$$

where k indexes the set of particles shown in Fig. 1 (b): f_k is the absorption, n_k the number density, $\langle \mathcal{E}_k \rangle$ the ensemble-averaged energy, and v_k the velocity associated with particles of the k^{th} type. f is the total absorption,

\mathcal{R} is the reflectivity, and $u_1 = a_0^2 m c^2 n_c / 2$ is the energy density of the laser.

The coupling between strong-field QED and laser-produced dense plasma is illustrated in Fig. 1 (b). The classical portion of the interaction involves deposition of laser energy into electrons and ions as is shown using blue arrows. QED processes, indicated using green arrows, redistribute energy coupled into relativistic electrons first through the emission of quantum synchrotron γ -rays by propagation in the laser field. QED corrections to the electron absorption are thus introduced as the Lorentz-invariant quantum parameter,

$$\chi = \frac{\gamma}{E_{Sch}} \sqrt{(\mathbf{E} + \mathbf{v} \times \mathbf{B})^2 - (\mathbf{E} \cdot \mathbf{v}/c)^2}, \quad (2)$$

reaches ~ 0.1 (\mathbf{B} is the laser’s magnetic field, $E_{Sch} = 1.3 \times 10^{18} \text{ V m}^{-1}$ is the critical field of QED [22]). Production of electron-positron pairs takes place when $\chi \sim 1$ through γ -ray conversion in the laser fields themselves which is controlled by the quantum parameter $\chi_\gamma = \hbar\omega/(2mc^2 E_{Sch}) |\mathbf{E}_\perp + \hat{\mathbf{k}} \times c\mathbf{B}|$, where the photon has energy $\hbar\omega$ and propagates along the $\hat{\mathbf{k}}$ unit vector, and \mathbf{E}_\perp is the component of the laser electric field normal to its motion. The γ -ray absorption is thus set by the leptonic radiative energy loss and the positrons take an n_+/n_e fraction of the total pair energy which is always less than $\frac{1}{2}$.

II. ABSORPTION MODEL

A. Classical Relativistic Absorption

At the petawatt scale, the theoretical extrema of f in the supercritical situation have recently been reported using a kinematic interaction model. This works by applying shockwave-like conservation laws across the supercritical interface to constrain f in relation to the laser and unperturbed matter properties [18, 19]. In this section we review the essential results and extend them to the situation of interest here.

Denoting the absence of QED using a superscript 0, the sets of all possible f -curves associated with eq. (1) are given by

$$\begin{aligned} f_i^0 &= \frac{2\beta\mathcal{R}^{3/2}}{\sqrt{\beta^2\mathcal{R}+1}-\beta\sqrt{\mathcal{R}}} \\ f_e^0 &= \frac{(1-\mathcal{R})\sqrt{\beta^2\mathcal{R}+1}-(1+\mathcal{R})\beta\sqrt{\mathcal{R}}}{\sqrt{\beta^2\mathcal{R}+1}-\beta\sqrt{\mathcal{R}}} + O\left(\frac{\rho_e}{\beta^2}\right). \end{aligned} \quad (3)$$

Here $f^0 = f_e^0 + f_i^0$ where the terms correspond to electrons and ions, respectively. These limits bound the efficiency of nonlinear absorption mechanisms operating in petawatt-scale laser interactions with supercritical matter [23–26], while effects occurring downstream of the interface such as efficient plasma wave heating of dense matter [27, 28] are abstracted from the analysis.

As a consequence, the nonlinear plasma dynamical interaction is parameterized by three control variables: $\rho_e = n_e/n_i m/(M + Zm) \ll 1$, corresponding to the normalized mass density of relativistic electrons accelerated by the laser, the reflectivity \mathcal{R} , and the dimensionless velocity $\beta = [Zmn_c/(2Mn_0)]^{1/2}a_0$, and the supercritical interface has uniform charge-state Z , and ion density $n_i = Zn_0$ and mass M . We note that a_0 corresponds to the peak laser dimensionless strength parameter, so the laser-cycle-averaged value often used in classical laser interactions is recovered by $a_0 \rightarrow \sqrt{2}a_0$. The dimensionless velocity of the supercritical interface is given by [18, 19]

$$\beta_{\text{hb}} = \sqrt{\frac{\mathcal{R}\beta^2}{1 + \mathcal{R}\beta^2}}. \quad (4)$$

The laser temporal envelope is constrained by $I (\partial I/\partial t)^{-1} \gg 2\pi \omega_{\text{pe}}^{-1}$ which is readily achieved in realistic conditions, where the electron plasma frequency $\omega_{\text{pe}} = (n_0 e^2/\epsilon_0 m)^{1/2}$. Damping of transient momentum effects also requires that the laser pulse duration τ satisfies $\tau \omega_{\text{pi}} > 2\pi C$ where the ion plasma frequency $\omega_{\text{pi}} = (Zn_0 e^2/\epsilon_0 M)^{1/2}$ for supercritical interface uniform charge-state Z , ion mass M , and $C \simeq 3 - 5$. The target thickness D should exceed the hole-boring depth and the effective relativistic electron refluxing range, $D > c[\tau/2 + \int_0^\tau \beta_{\text{hb}} dt]$ in order to access the steady-state interaction [18, 19]. The rate of electron heating

in the model is proportional to the scalar product of the particle velocity and electric field which scales linearly with a_0 . In the absence of radiative cooling this implies ponderomotive scaling of the electron energy [25, 29], *i.e.*, $\langle \mathcal{E}_e^0 \rangle = a_0 mc^2/\sqrt{2}$, which Fig. 3 shows is consistent with the energetics exhibited in our simulations.

To first order in ρ_e , the absorption is then given by,

$$f_e^0 \simeq \frac{1+\beta}{\beta^2} \left(\frac{3\sqrt{2}}{20}a_0 - 1 \right) \rho_e, \quad (5)$$

$$f_i^0 \simeq \frac{2\beta}{1+2\beta} - \frac{4\beta^2+7\beta+3}{2\beta(1+2\beta)^2} \left(\frac{3\sqrt{2}}{10}a_0 - 1 \right) \rho_e, \quad (6)$$

where the (laboratory frame) reflectivity $\mathcal{R} = 1 - f_e^0 - f_i^0$. When $a_0 \rightarrow 10\sqrt{2}/3$ the model suggests that absorption becomes asymptotically small. This implies that for $a_0 \lesssim 5$ in the supercritical situation the electron dynamics can be non-ponderomotive, as has been suggested in previous works [23, 30, 31]. We consider higher intensities in the present work which means that the supercritical plasma comprising the interface reaches a fully-ionized state and eqs. (5) and (6) are controlled by a_0 and the $\rho_e \propto n_e/n_0$ parameter alone. Interactions between $a_0 < 1$ laser light and opaque matter involve collisional dynamics [32] and are outside the scope of this work, as the threshold for a high-power laser interaction is set by $a_0 \geq 1$ when the oscillatory velocity of a free electron approaches c .

B. Strong-Field QED Processes

Inspection of eq. (2) reveals the crucial role played by the reflected laser wave, since a single laser pulse will accelerate electrons from rest such that they co-propagate along the direction of the light wavevector. In this situation the electric and magnetic forces acting on the electron approximately cancel one another – which leaves $\chi \ll 1$ for all foreseeable laser systems [10].

However, this picture changes substantially when the partially-reflected wave is treated. We work in the frame of reference co-propagating with the supercritical interface at $\beta_{\text{hb}}c$, meaning that the supercritical matter is injected into the laser fields with axial velocity $-\beta_{\text{hb}}c$, the surface has reflectivity $\mathcal{R}_{\text{hb}} = \mathcal{R}(1 + \beta_{\text{hb}})/(1 - \beta_{\text{hb}})$, the incident and reflected waves have frequency $\omega_{\text{hb}} = \omega[(1 + \beta_{\text{hb}})/(1 - \beta_{\text{hb}})]^{-1/2}$. At focus the laser spot size is much larger than the wavelength λ and we assume the laser ponderomotive force rapidly sweeps away any underdense pre-plasma associated with the production of the laser pulse for the ultra-high intensities of interest here [33]. The electric and magnetic fields in the vacuum region are given by,

$$\begin{aligned} \frac{eE_x}{mc\omega_{\text{hb}}} &= a_0 \left[\cos(\xi - \tau) - \sqrt{\mathcal{R}_{\text{hb}}} \cos(\xi + \tau) \right], \\ \frac{eB_y}{m\omega_{\text{hb}}} &= a_0 \left[\cos(\xi - \tau) + \sqrt{\mathcal{R}_{\text{hb}}} \cos(\xi + \tau) \right], \end{aligned} \quad (7)$$

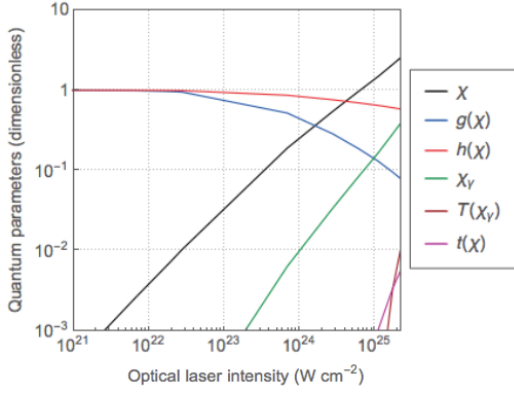


FIG. 2. **Quantum parameters controlling particle production.** Quantum corrections to absorption become important when the Lorentz-invariant parameters χ and $\chi_\gamma \gtrsim 0.1$. χ compares the electric field strength in the rest frame of a lepton to the quantum critical field [22]. Leptons emit $N_\gamma \propto \chi h(\chi)$ photons per unit time and lose energy at a rate of $\mathcal{P} \propto \chi^2 g(\chi)$. $h(\chi)$ and $g(\chi)$ thus describe quantum corrections to the photon spectrum which affect the classical emissivities. χ_γ controls the probability for a γ -ray to convert into an electron-positron pair by direct interaction with the laser fields. Pair creation is suppressed for $\chi_\gamma \lesssim 0.1$, but becomes exponentially more probable as χ_γ increases, leading to a “cascade” of self-created particles when $\chi_\gamma \gtrsim 1$. Its exponential growth is parameterized by the auxiliary function $T(\chi_\gamma)$ in the pair creation rate, and $t(\chi)$ approximates $T(\chi_\gamma)$ with χ_γ weighted over the emission spectrum (details provided in the text).

defining the dimensionless axial distance $\xi = \omega_{\text{hb}} z/c$ and time $\tau = \omega_{\text{hb}} t$.

n_e electrons escape the bulk plasma and enter the vacuum region where the partial standing wave can accelerate them to relativistic energy, radiating γ -rays if a_0 is large enough. For $\mathcal{R}_{\text{hb}} = 1$, $z = -\lambda/4$ is a node of the magnetic field and an antinode of the electric field. The electron is accelerated parallel to the electric field, so χ vanishes and it reaches a peak momentum of $\sim 2a_0 mc$ [24, 25]. However, the $B = 0$ node is unstable – if the electron starts slightly off-node, it is pushed towards the electric field node. This suggests only particles within the region $-\lambda/4 \lesssim z \lesssim \lambda_p$ are heated by the wave, meaning that absorption is highly localized with an axial lengthscale less than λ .

We assume the electron is ultrarelativistic with $v = c$, and that the electric and magnetic forces perpendicular

to its motion are almost in balance. The particle’s relativistic motion means its period of oscillation is much longer than the laser period. Furthermore, due to the localization, the wave phase interval in which it is accelerated is very small. As a consequence of this, averaged over the wave phase, we can anticipate a steady-state solution for the absorption. Confining the electron motion to the x - z plane, force balance in the perpendicular direction gives $E_x \cos \theta \simeq cB_y$ where θ corresponds to the angle of the electron’s acceleration relative to the laser axis. This defines the trajectory by $d\xi/d\tau = cB_y/E_x$, with boundary condition that $\xi = -\pi/2$ at $\tau = \pi$. Substituting $\xi = -\pi/2 + \cos \theta(\tau - \pi)$ into the field definitions given by equation (7) and expanding around $\tau = \pi$, we find that the electrons are initially accelerated at an angle $\cos \theta = (1 - \mathcal{R}_{\text{hb}}^{1/4})/(1 + \mathcal{R}_{\text{hb}}^{1/4})$. This angle cannot be sustained indefinitely – the magnetic field increases along this trajectory and therefore the electron should be deflected toward the supercritical interface. We make the further approximation that the electron propagates at this angle until such a time that $E_x(\tau, \xi) = cB_y(\tau, \xi)$. Thereafter it moves parallel to the laser axis until it crosses the interface at $\xi = 0$.

In reality, the complex nature of the fields and the stochastic nature of photon emission mean that the electron will deviate from the balanced trajectory – nevertheless, this rectilinear model should suffice to describe the most important physics.

1. Quantum γ -ray Radiation

The instantaneous average power radiated to photons by an electron (or positron) is $\mathcal{P} = (2\alpha/3\tau_c)\chi^2 g(\chi)mc^2$, where $\alpha \simeq 1/137$ is the fine structure constant, $\tau_c = \hbar/mc^2$ is the Compton time and the auxiliary function $g(\chi)$ is the factor by which quantum corrections reduce the radiated power [34, 35]. Although the fact that photon emission is a stochastic process means $\chi(\tau)$ does not change smoothly over the interval $\tau \in [\pi, \tau(\xi = 0)]$, it is possible to use the average power to determine the average radiated energy [35], by $\langle \mathcal{E} \rangle = \int \mathcal{P}(\langle \chi \rangle) d\tau$.

Assuming for the present $\langle \mathcal{E}_e^0 \rangle = a_0 mc^2/\sqrt{2}$ is constant over the electron motion, the quantum parameter is given by $\chi(\tau) = a_0 |cB_y - E_x \cos \theta|/(\sqrt{2}E_{\text{Sch}})$. Squaring and integrating this along the electron trajectory defines the root-mean-square (r.m.s.) χ_{rms} by $\int \chi^2 d\tau \equiv \chi_{\text{rms}}^2 \Delta\tau$, yielding,

$$\chi_{\text{rms}} = \frac{a_0^2}{\pi} \frac{\hbar\omega \sqrt{\frac{1-\beta_{\text{hb}}}{1+\beta_{\text{hb}}}}}{mc^2} \left\{ \frac{2r^2[\pi(1+r^3-r^5-r^6) - 4r \sin(\pi r)]}{(1-r)(1+r)^2(1+2r)^2} - \frac{r(1+r^3+r^4) \sin(2\pi r)}{(1+r)(1+2r)^2} \right\}^{1/2}, \quad (8)$$

where $r^4 \equiv \mathcal{R}_{\text{hb}}$ and ω is the laser angular frequency in

the laboratory frame. As can be seen in Fig. 2, χ is suf-

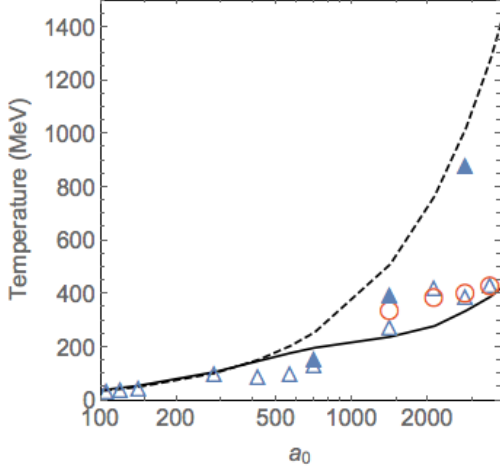


FIG. 3. **Electron and positron temperature scalings.** Simulation results are shown for electrons using blue markers and positrons using red markers. The filled symbols correspond to simulations in which the QED module was deactivated and the open symbols to simulations in which the QED module was activated. The dashed black curve corresponds to the ponderomotive temperature scaling [29] and the solid black curve to the cooled lepton temperature scaling given by eq. (9).

ficiently large that $g(\chi)$ gives a non-negligible correction to the radiated intensity. We include this by using χ_{rms} to define an average $\langle g \rangle \equiv g(\chi_{\text{rms}})$ with which we scale the radiated energy.

To account for the recoil of the electron, we consider the evolution equation $\gamma'(\tau) = -A\gamma^2$, since $\chi \propto \gamma$. Assuming A to be constant and defining $\gamma_0 \equiv \gamma(\tau = 0)$ means that $\gamma(\tau) = \gamma_0/(1 + A\gamma_0\tau)$. We can identify $A\gamma_0^2\tau$ with the radiated energy in absence of recoil $\langle \mathcal{E}_{\gamma, \text{hb}} \rangle$ and therefore calculate the recoil-corrected quantities as

$$\chi_{\text{rms}}^{\text{recoil}} = \frac{\chi_{\text{rms}}}{\sqrt{1 + \langle \mathcal{E}_{\gamma, \text{hb}} \rangle / \langle \mathcal{E}_e^0 \rangle}}, \quad (9)$$

$$\langle \mathcal{E}_{\pm} \rangle = \frac{\sqrt{\frac{1+\beta_{\text{hb}}}{1-\beta_{\text{hb}}}} \langle \mathcal{E}_e^0 \rangle}{1 + \langle \mathcal{E}_{\gamma, \text{hb}} \rangle / \langle \mathcal{E}_e^0 \rangle}. \quad (10)$$

$\langle \mathcal{E}_{\pm} \rangle$ corresponds to the radiatively-cooled e^-/e^+ energy and the Doppler factor accounts for the transformation from the co-propagating to laboratory frame; the radiated energy in the absence of recoil is given by,

$$\langle \mathcal{E}_{\gamma, \text{hb}} \rangle = \frac{\pi\alpha}{3} (1 + 2r) \chi_{\text{rms}}^2 \langle g \rangle \frac{(mc^2)^2}{\hbar\omega \sqrt{\frac{1-\beta_{\text{hb}}}{1+\beta_{\text{hb}}}}}. \quad (11)$$

We compare this expression for the temperature with the ponderomotive prediction and with simulation data in Fig. 3.

2. Electron-Positron Pair Production

The differential probability rate for a γ -ray photon, travelling at an angle θ to the laser axis, to convert to an electron-positron pair via the multi-photon Breit-Wheeler process [36, 37] is given by

$$\frac{dP_{\pm}}{dt} = \frac{\alpha}{\tau_c} \frac{mc^2}{\hbar\omega} \chi_{\gamma} T(\chi_{\gamma}) \quad (12)$$

$T(\chi_{\gamma})$ is the Breit-Wheeler auxiliary function which is well approximated as [36, 38],

$$T(\chi_{\gamma}) \simeq \frac{0.16}{\chi_{\gamma}} K_{1/3}^2 \left(\frac{2}{3\chi_{\gamma}} \right) \quad (13)$$

where K is the modified Bessel function of the second kind. On the other hand, second-order pair production via virtual photons in the Trident process is strongly suppressed in the laser-plasma context and is negligible for our purposes [39]. $T(\chi_{\gamma})$ in equation (12) should be weighted using the full synchrotron spectrum, *i.e.*, using the transformation,

$$T(\chi_{\gamma}) \rightarrow \int_0^{\chi_{\gamma}^{1/2}} \frac{F(\chi, \chi_{\gamma}) T(\chi_{\gamma})}{h(\chi) \chi_{\gamma}} d\chi_{\gamma} \quad (14)$$

so that the photon spectrum is characterized by χ of the radiating electron. The integral in equation (14) in general must be evaluated numerically, but over the range $0 \leq \chi \leq 10$ the following analytical approximation differs from the true value by at most 5%:

$$t(\chi) \simeq \frac{3}{16} \exp \left(-\frac{114}{37\sqrt{\chi}} - \frac{71}{18\chi} - \frac{1}{19\chi^2} \right) \quad (15)$$

The intensity scalings of χ_{γ} and the auxiliary functions eqs. (14) and (15) are shown in Fig. 2.

The average angle between γ -ray wavevector and the laser axis is given by $\cos \langle \theta_{\gamma, \text{hb}} \rangle \simeq \sqrt{3}(1 - \mathcal{R}_{\text{hb}})/2$. Together with the fact that $\chi_{\text{rms}}^{\text{recoil}}$ characterizes the shape of the photon spectrum, we can integrate the photon conversion rate along the trajectory defined by this angle to obtain the pair creation probability

$$P_{\pm} \simeq \frac{\alpha a_0 \mathcal{R}_{\text{hb}}^{3/4} (1 - \mathcal{R}_{\text{hb}} + 2/\sqrt{3}) t(\chi_{\text{rms}}^{\text{recoil}})}{(1 - \mathcal{R}_{\text{hb}}) (1 + \mathcal{R}_{\text{hb}}^{1/4})}. \quad (16)$$

For γ -ray number density n_{γ} , equation (16) controls the positron density according to $n_+/n_0 = P_{\pm} n_{\gamma}/n_0$. n_{γ} is obtained by integrating the emission rate along the electron trajectory and then scaling by the number of electrons that have escaped the bulk matter:

$$\frac{n_{\gamma}}{n_0} = \frac{n_e}{n_0} \frac{5\alpha}{2\sqrt{3}} a_0 [1 - r^2 - (1 + r^2) \cos(\pi r)] \frac{h(\chi_{\text{rms}}^{\text{recoil}})}{5\pi/3}. \quad (17)$$

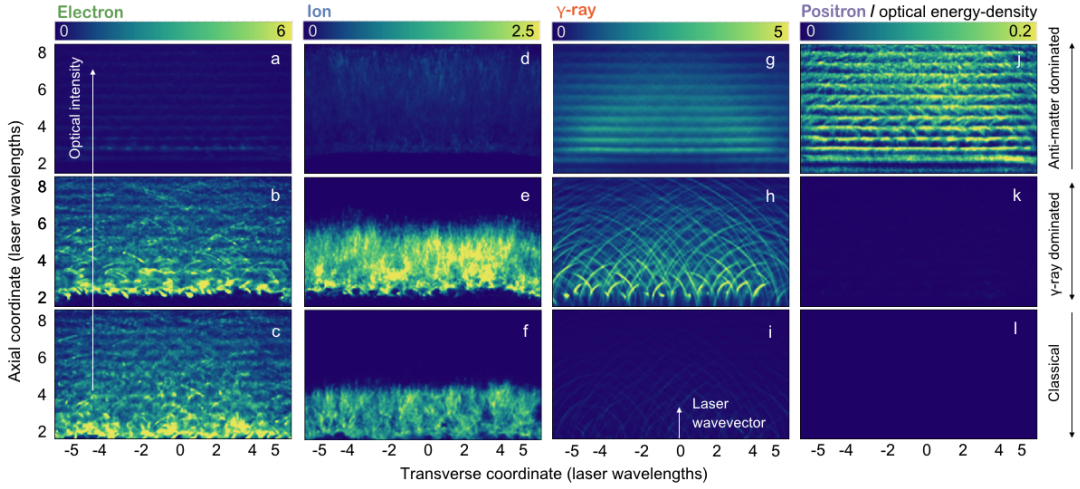


FIG. 4. **Particle production.** Snapshots are shown of the normalized spatial energy-density of electrons, ions, γ -rays, and positrons. Regimes of particle production are illustrated by varying the optical intensity from $6.5 \times 10^{23} \text{ W cm}^{-2}$, to $2.6 \times 10^{24} \text{ W cm}^{-2}$, and $1.7 \times 10^{25} \text{ W cm}^{-2}$ (rows, bottom to top). Thin, high energy-density radial filaments of γ -rays are created (h) through quantum synchrotron cooling of electrons (b) which penetrate the surface plasma layer into the ultra-strong laser field twice each optical cycle. Positron production through γ -ray decay (j-l) and collimation of γ -ray emission along the laser wavevector increase with intensity. As a consequence, the normalized γ -ray energy-density peaks around (h) then decreases with intensity, as is shown in (g). All parameters are detailed in the text.

C. Feedback Between QED and Classical Dynamics

QED processes have the effect of redistributing energy initially coupled by the laser into relativistic electrons. Normalized to the classical electron value, the γ -ray absorption is set by the radiative energy loss of e^\pm as $f_\gamma = (1 - \langle \mathcal{E}_\pm \rangle / \langle \mathcal{E}_e^0 \rangle) f_e^0$. The complement of this corresponds to the total e^\pm absorption accounting for γ -ray emission as $f_e + f_+ = \langle \mathcal{E}_\pm \rangle / \langle \mathcal{E}_e^0 \rangle f_e^0$. Positrons take an n_+/n_e fraction of the total pair energy which is always less than $\frac{1}{2}$ as $f_+ = P_\pm (n_\gamma/n_e) (\langle \mathcal{E}_\pm \rangle / \langle \mathcal{E}_e^0 \rangle) f_e^0$.

Fig. 3 shows that electrons in the no-QED simulations are accelerated to approximately the ponderomotive potential [29], in good agreement with the classical absorption model. With QED effects present, the highest energy γ -rays are converted by the laser fields into “daughter” electrons and positrons which each gain approximately half the parent lepton’s energy. The daughter particles are re-accelerated to $\langle \mathcal{E}_e^0 \rangle$ and cool to $\langle \mathcal{E}_\pm \rangle$ in steady-state. There is also close agreement between the QED simulation results and the model predictions for $\langle \mathcal{E}_\pm \rangle$ given by eq. (9) for both positrons and electrons.

Equilibration with electrons extracted from the target can be understood by considering the work done on the self-created pairs by the laser field through $d\mathcal{E}/dt = e\mathbf{v} \cdot \mathbf{E}$. We assume for simplicity acceleration parallel to the laser electric field in the hole-boring frame and energy $\mathcal{E} \gg m_e c^2$. The timescale τ_{accel} for acceleration to the ponderomotive energy can then be estimated as $\langle \mathcal{E}_e^0 \rangle / (2\tau_{\text{accel}}) \sim m_e c^2 a_0 \omega_{\text{hb}}$, which yields $\tau_{\text{accel}} \sim 1/(2\sqrt{2}\omega_{\text{hb}})$.

The timescale associated with radiative cooling [5],

τ_γ , is proportional to $1/W_{e \rightarrow \gamma}$ where $dW_{e \rightarrow \gamma}/d\chi_\gamma = \sqrt{3}\alpha\chi F(\chi, \chi_\gamma)/(2\pi\tau_c\gamma\chi_\gamma)$ corresponds to the differential rate of photon emission [5, 36, 40]. Integrating over all photon energies in the range $0 \leq \chi_\gamma \leq \chi/2$ using $\gamma = a_0/\sqrt{2}$ gives the total emission rate to be $W_{e \rightarrow \gamma} = \sqrt{3/2}\alpha\chi h(\chi)/(\pi a_0 \tau_c)$. Using χ and $h(\chi)$ as given in Fig. 2, $\tau_{\text{accel}} \lesssim \tau_\gamma$ for all values of a_0 below the pair cascade. A characteristic of S (“shower”) type pair cascades is that daughter positrons are much cooler than the parent particles due to energy partitioning. By contrast, these results indicate that electrons and positrons reach comparable energies, providing a signature of re-acceleration and hence an A (“avalanche”) type cascade process [41].

Creation of prolific pairs in the absorption region not only provides new sources of current, but ultimately also screens the supercritical matter from the incident electromagnetic wave. When the density of these self-created particles exceeds the relativistically critical density, the electromagnetic fields responsible for QED processes are damped as,

$$a_0 \rightarrow a_0 \sqrt{a_0 n_c / (n_0 + 2n_+)} = a_0 / \sqrt{1 + 2P_\pm n_\gamma / n_0}, \quad (18)$$

where the pair creation probability P_\pm relates the γ -ray number density n_γ to the positron density n_+ according to $n_+/n_0 = P_\pm n_\gamma / n_0$. The normalized lepton density effectively grows by

$$n_e/n_0 \rightarrow n_e/n_0 (1 + 2P_\pm n_\gamma / n_0). \quad (19)$$

The secondary effect of the increasing electron and positron mass density on the ions will be described in

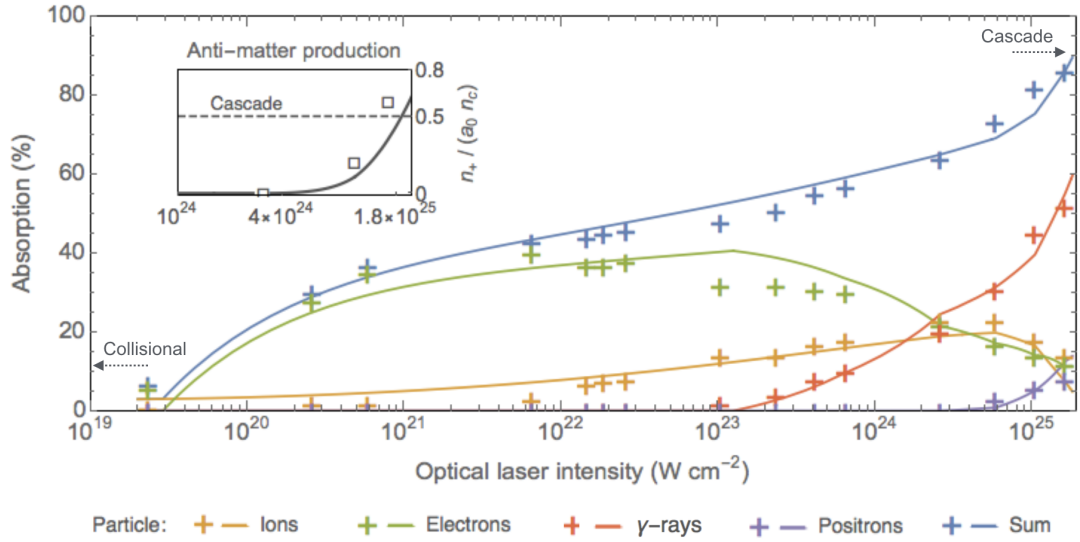


FIG. 5. **Absorption across all optical intensity scales.** The quantum conversion efficiency of intense photon flux into energetic particles via absorption is presented across six orders-of-magnitude in optical laser intensity (solid – model and markers – data from massive-scale QED-PIC simulations [42]). A cascade of electron-positron pairs reaching 4×10^{24} positrons cm^{-3} is triggered by highly-efficient γ -ray production at $1.8 \times 10^{25} \text{ W cm}^{-2}$. Mass of the self-created particles accumulates at the interface between the laser and quantum electrodynamical plasma to produce an inflection in ionic absorption at $5 \times 10^{24} \text{ W cm}^{-2}$.

the following section.

III. COMPARISON TO QED-PIC SIMULATION RESULTS

We use the classical value of $n_e/n_0 = 0.3$ to facilitate comparison to the simulation results. Since n_0 is scaled linearly with a_0 to satisfy the optically-thick condition, $n_e/n_0 = \text{const.}$ is consistent with the well-known S -scaling of electron dynamics [21, 43]. This quantity corresponds to the fraction of electrons which escape the bulk matter and are accelerated by the laser to relativistic energies and is the only free parameter of the model. Deriving it *ab initio* is a long-standing topic of interest in the field of high-power laser-plasma physics which is beyond the scope of the present work. We find the absorption model best matches the simulation data when this is equal to 0.3, well within the range of values $\simeq 0.1 - 0.5$ typically reported in the literature [31, 44, 45].

In Fig. 4 snapshots are shown of the normalized spatial energy-density of electrons, ions, γ -rays, and positrons which illustrate the classical to QED plasma transition.

Fig. 5 quantitatively compares predictions of the absorption model to 15 high-resolution multidimensional QED-PIC simulation [42] results. Extending to the optical intensity in which γ -rays are first produced, around $10^{23} \text{ W cm}^{-2}$, the model is seen to accurately describe classical relativistic laser-matter interactions, reproducing the well-known S -scaling of electron dynamics [21] while also correctly accounting for ion dynamics. In the intensity interval from $10^{23} \text{ W cm}^{-2}$ to $3 \times 10^{24} \text{ W cm}^{-2}$,

where the first positrons are produced (in close agreement with the $\chi \sim 1$ region shown in Fig. 2), the total absorption less that taken by the ions is constant to within a few percent which confirms the model's picture of energy flow as depicted in Fig. 1. While both n_+/n_0 and $f_+ < 0.01$, this intensity scale is within a factor of order-unity of the value first suggested in Bell and Kirk [10].

Above this intensity, our findings show that the effect of profic pair creation is to increase the energy absorbed as γ -rays, as the self-created leptons accelerate and radiatively cool in the same way as electrons originating in the plasma layer. In addition, the mass of these particles accumulates at the interface between the laser and QED plasma. As a consequence of the self-created inertia, the interface velocity β_{hb} slows and an inflection in the ion absorption is produced. This novel QED plasma dynamic which connects lepton creation to ion acceleration emerges naturally from the absorption model due to kinematic coupling of electrons and ions [18, 19] and points to an optimal parameter space for future QED ion acceleration schemes. The absorption curves shown in Fig. 5 thusly elucidate how optically-thick matter responds to laser illumination by creation and acceleration of particles across six orders-of-magnitude in optical intensity.

While integration over the QED rates must in general be carried out numerically, our results can be closely approximated in terms of I_{18} , the laser's intensity in units

of $10^{18} \text{ W cm}^{-2}$, as,

$$f = 9.9 \times 10^{-5} I_{18}^{1/2} - \frac{2.6}{I_{18}^{1/2}} + 0.48 \quad (20)$$

$$f_i = -4.7 \times 10^{-12} I_{18}^{3/2} + 7.6 \times 10^{-5} I_{18}^{1/2} - \frac{0.96}{I_{18}^{1/2}} + \frac{3.3}{I_{18}^{0.96}} + 0.087 \quad (21)$$

$$f_e = 3.1 \times 10^{-12} I_{18}^{3/2} - 1.3 \times 10^{-4} I_{18}^{1/2} - \frac{1.3}{I_{18}^{0.34}} + 0.45 \quad (22)$$

$$f_\gamma = 1.3 \times 10^{-13} I_{18}^{3/2} + 1.4 \times 10^{-4} I_{18}^{1/2} + \frac{2.3}{I_{18}^{1.3}} - 0.015 \quad (23)$$

$$f_+ = 2.1 \times 10^{-12} I_{18}^{3/2} - 6.1 \times 10^{-6} I_{18}^{1/2} + \frac{0.21}{I_{18}^{1.9}} + 1.4 \times 10^{-3} \quad (24)$$

where the R^2 value associated with each curve is 0.99. Processes occurring $> \lambda_p$ downstream from the laser-matter interface are abstracted from this analysis [18, 19]. Equations (20) to (24) for f, f_k therefore provide initial conditions to all current and future modeling efforts which make use of dense laser-driven particle beams.

The solid target effectively vanishes behind a screen of self-created particles when the pair density approaches the initial electron density. To assess this Fig. 5 (inset) compares the model-predicted n_+ to the positron density near the supercritical interface measured directly in the simulations. Agreement better than 10% is observed all the way to the electron-positron pair cascade at $1.8 \times 10^{25} \text{ W cm}^{-2}$. In this optical field the positron production achieves $4 \times 10^{24} \text{ cm}^{-3}$, providing an anti-matter source $10^6 \times$ denser than of any known photonic scheme [46, 47]. Furthermore, since the triggering of a pair cascade is believed to set an ultimate upper limit on attainable electromagnetic field intensity [5, 6], these findings offer further insights into how the ubiquitous scenario of light absorption/reflection from opaque matter will work in the most extreme conditions which could ever be achieved on Earth.

IV. CONCLUSION

We have shown that by coupling strong-field QED to a classical kinematic theory of laser-matter interactions, we may predict the optically-thick absorption to electrons, ions, γ -rays and positrons across all high-power laser intensity scales. The model, verified by massive-scale QED-PIC simulations, demonstrates novel features of the plasma response which arise only because of this coupling. At ELI intensities [2], the bulk of the laser energy is absorbed to γ -rays, leading to the production of pair plasmas so dense that self-created lepton inertia slows the velocity of the interface between vacuum and matter.

The ion absorption reaches a maximum which reveals optimal parameter space for ultra-high-field ion accelerator applications. These findings thereby lay the groundwork necessary to understand how dense laser-driven particle beams can be applied to radiotherapy [48–50] at the petawatt-scale, to the study of nuclear interactions with high density γ -rays [11, 51], and to scaled laboratory studies of black hole and pulsar winds [52, 53].

M. C. L. thanks Stephen B. Libby for useful discussions early in the project. M. C. L. thanks the Royal Society Newton International Fellowship for support, and the EPSRC Plasma High-End Computing Consortium and University of Oxford Advanced Research Computing (ARC) facility for computational resources. T. G. B. thanks the Knut and Alice Wallenberg Foundation (KAWF) for support. N. R. thanks the EPSRC for the support. C. P. R. acknowledges support from EPSRC grant number EP/M018156/1. A. I. thanks the KAWF and the Olle Engkvist Foundation, grant 2014-744. M. M. thanks the KAWF and Swedish Research Council, grants 2012-5644 and 2013-4248.

Appendix A: QED-PIC Simulations

The numerical simulations were carried out using the massively-parallel quantum electrodynamical particle-in-cell (QED-PIC) code EPOCH [35, 42]. EPOCH directly solves the fully-relativistically-correct Lorentz force equation and full set of Maxwell's equations, thus capturing the relevant kinetic physics of the classical high-power laser-matter interaction.

In EPOCH QED effects are coupled semi-classically to the PIC workings using a Monte-Carlo algorithm which describes quantum radiation emission and electron-positron pair production. The code implements the quasistatic and weak-field approximations to the QED rates, as described in [35], which are consistent with the laser-plasma situation. The separation of energy scales between the γ -ray photons produced by synchrotron emission and the (optical) photons associated with the high-power laser allows a treatment of the stochastic processes according to the model of Baier and Katkov [54].

We have carried out 15 multidimensional simulations using laser and supercritical matter conditions consistent with the above, over the intensity interval $\sim 10^{19} - 10^{25} \text{ W cm}^{-2}$. The code is configured to run in two spatial dimensions for computational efficiency with a simulation box size of 40λ in the transverse x coordinate and 40λ in the axial z coordinate, each running from -20λ to 20λ , where the laser wavelength is $\lambda = 1 \mu\text{m}$. The simulation is assumed to be uniform in the y direction, mimicking a laser spot with spatial extent in y much greater than λ .

The simulations use a high-power laser pulse whose intensity is varied across 15 values in the range of $\sim 10^{19} - 10^{25} \text{ W cm}^{-2}$. The beam is linearly-polarized in the simulation plane and modeled using a 8th-order

super-Gaussian (*i.e.*, square) transverse spatial profile, with spot diameter at focus of $2r_l = 16\mu\text{m} \gg \lambda$. The temporal profile of the laser is modeled using a 4th-order super-Gaussian centered at 50 fs with a full-width half-max of 40 fs.

The interaction is simulated for 50 τ_l (optical cycles) which captures the rise and fall of the laser pulse and confirms that a steady-state of absorption – in which $df_k/d\tau_l \simeq 0$ where f_k is the absorption into the k^{th} particle type as defined in equation (1) – is reached.

The supercritical target is modeled as a fully-ionized slab of cold plasma having electron density $1.01\sqrt{2}a_0n_c$ with ion charge-to-mass ratio $Z/A = 1$. We have confirmed the matter is opaque to the high-power laser light, as it should be. The slab is situated within $0 \leq z/\lambda \leq 19$ and $|x/\lambda| \leq 19$. The 1λ margin of vacuum is maintained along each coordinate in order to mitigate any numerical effects related to the simulation boundaries, which are configured to transmit electromagnetic radiation and particles.

To facilitate comparison to the model we use the classical $n_e/n_0 = 0.3$ and the \mathcal{R} and β_{hb} quantities measured directly in the simulations in Fig. 5.

The following steps have been taken to ensure that the numerical methods used in the simulations result in an accurate description of the physics. The simulation timestep is determined by the Courant condition multiplied by a factor of 0.5 which enhances stability. The spatial resolution is 20 cells/ λ along both spatial coordinates, corresponding to 3 cells/ λ_p where the plasma relativistic collisionless skin depth $\lambda_p = a_0^{1/2}c/\omega\sqrt{n_c/n_0}$ (where c is the speed of light, n_0 is the initial plasma electron density, $n_c = \varepsilon_0 m \omega^2 / e^2$ is the critical density, ω is the laser angular frequency, m is the electron mass, ε_0 is the vacuum permittivity, and e is the fundamental charge). Therefore all relevant physical scales are resolved. We have confirmed that the simulation results for all quantities of interest have converged using this resolution.

Due to the well-known infrared divergence of the photon emission rate, EPOCH allows the specification of a

lower-limit energy for photon particles to be cast to the simulation grid. This cutoff is taken to be 50 keV, for which we have confirmed that the absorption values converge.

The code is configured to operate in collisionless mode, since the collisional mean-free path of relativistic particles in the vacuum absorption region we are interested in is much longer than the region scale-size. To confirm this, we have carried out several collisionless simulations and found no appreciable difference in the quantities of interest.

Particles are fully kinetic and are represented using 210 electrons per cell and 90 ions per cell, meaning there are $\sim 10^8$ macroparticles in the simulations at the initial timestep. The higher mass of the ions means they can be efficiently modeled using fewer particles, and the particle weighting has been adjusted to preserve charge neutrality at $t = 0$ in the simulation. We have carried out an extensive survey of conditions and verified that all quantities of interest converge using this value.

The diagnostic which is used to calculate the absorption in the simulations tracks the cumulative kinetic energy coupled into each of the k particle species over time. These values are normalized to the total field energy injected into the simulation box for an “empty” run which is absent the supercritical target. Following the interaction between the laser and matter, which occurs at around 150 fs due to the hydrodynamic effect, this procedure directly yields a clean measurement for f_k . For the steady-state interaction this has been demonstrated in previous works to be exactly equivalent to equation (1) of the main manuscript text [18, 19].

The particle temperatures are calculated using the reciprocal slope of a fit-line matched to the quasi-exponential portion of the energy distribution at 130fs. The hole-boring velocity $\beta_{\text{hb}}c$ is calculated by tracking the supercritical interface at the simulation midplane $x = 0$ during the steady-state laser-plasma interaction from 100-130 fs. The supercritical interface axial location z_{hb} is defined by $\sqrt{2}a_0n_c/n_0 = 1$ so the velocity of the interface is calculated as $\beta_{\text{hb}}c = dz_{\text{hb}}/dt$.

-
- [1] D. Strickland and G. Mourou, *Optics Communications* **56**, 219 (1985).
 - [2] “ELI - extreme light infrastructure,” (2014).
 - [3] M. Marklund and P. K. Shukla, *Reviews of Modern Physics* **78**, 591 (2006), [arXiv:0602123 \[hep-ph\]](#).
 - [4] A. Di Piazza, C. Müller, K. Z. Hatsagortsyan, and C. H. Keitel, *Reviews of Modern Physics* **84**, 1177 (2012).
 - [5] A. Fedotov, N. Narozhny, G. Mourou, and G. Korn, *Physical Review Letters* **105**, 1 (2010).
 - [6] S. Bulanov, T. Esirkepov, A. Thomas, J. Koga, and S. Bulanov, *Physical Review Letters* **105**, 1 (2010).
 - [7] T. Grismayer, M. Vranic, J. L. Martins, R. A. Fonseca, and L. O. Silva, *Phys. Plasmas* **23**, 056706 (2016).
 - [8] N. Neitz and a. Di Piazza, *Physical Review Letters* **111**, 1 (2013), [arXiv:arXiv:1301.5524v1](#).
 - [9] T. G. Blackburn, C. P. Ridgers, J. G. Kirk, and A. R. Bell, *Physical Review Letters* **112**, 015001 (2014).
 - [10] A. Bell and J. Kirk, *Physical Review Letters* **101**, 200403 (2008).
 - [11] C. Ridgers, C. Brady, R. Ducloux, J. Kirk, K. Bennett, T. Arber, a. Robinson, and a. Bell, *Physical Review Letters* **108**, 1 (2012).
 - [12] a. Benedetti, R. Ruffini, and G. Vereshchagin, *Physics Letters A* **377**, 206 (2013).
 - [13] L. L. Ji, a. Pukhov, E. N. Nerush, I. Y. Kostyukov, B. F. Shen, and K. U. Akli, *Physics of Plasmas* **21** (2014), [10.1063/1.4866014](#).
 - [14] D. A. Serebryakov, E. N. Nerush, and I. Y. Kostyukov,

- Physics of Plasmas **22** (2015), 10.1063/1.4938206, arXiv:1508.05722.
- [15] R. Capdessus and P. McKenna, *Physical Review E* **91**, 1 (2015).
 - [16] E. N. Nerush and I. Y. Kostyukov, *Plasma Physics and Controlled Fusion* **57**, 035007 (2015).
 - [17] T. V. Liseykina, S. V. Popruzhenko, and A. Macchi, *New J. Phys.* **18**, 072001 (2016).
 - [18] M. C. Levy, S. C. Wilks, M. Tabak, and M. G. Baring, *Physics of Plasmas* **20**, 103101 (2013).
 - [19] M. C. Levy, S. C. Wilks, M. Tabak, S. B. Libby, and M. G. Baring, *Nature Communications* **5**, 1 (2014).
 - [20] A. Kemp and L. Divol, *Physical Review Letters* **109**, 195005 (2012).
 - [21] A. Pukhov, S. Gordienko, S. Kiselev, and I. Kostyukov, *Plasma Physics and Controlled Fusion* **46**, B179 (2004).
 - [22] W. Heisenberg and H. Euler, *Z. Phys* **98**, 714 (1936).
 - [23] M. Haines, M. Wei, F. Beg, and R. Stephens, *Physical Review Letters* **102**, 1 (2009).
 - [24] A. Kemp, Y. Sentoku, and M. Tabak, *Physical Review E* **79**, 066406 (2009).
 - [25] J. May, J. Tonge, F. Fiuza, R. a. Fonseca, L. O. Silva, C. Ren, and W. B. Mori, *Physical Review E* **84**, 025401 (2011).
 - [26] G. E. Kemp, a. Link, Y. Ping, D. W. Schumacher, R. R. Freeman, and P. K. Patel, *Physics of Plasmas* **20**, 033104 (2013).
 - [27] E. Lefebvre and G. Bonnaud, *Physical Review E* **55**, 1011 (1997).
 - [28] M. Sherlock, E. G. Hill, R. G. Evans, S. J. Rose, and W. Rozmus, *Phys. Rev. Lett.* **113**, 255001 (2014).
 - [29] S. C. Wilks, W. L. Kruer, M. Tabak, and A. B. Langdon, *Physical Review Letters* **69**, 1383 (1992).
 - [30] F. N. Beg, a. R. Bell, a. E. Dangor, C. N. Danson, a. P. Fews, M. E. Glinsky, B. a. Hammel, P. Lee, P. a. Norreys, and M. Tatarakis, *Physics of Plasmas* **4**, 447 (1997).
 - [31] T. Kluge, T. Cowan, A. Debus, U. Schramm, K. Zeil, and M. Bussmann, *Physical Review Letters* **107**, 205003 (2011).
 - [32] S. C. Wilks and W. L. Kruer, *IEEE Journal of Quantum Electronics* **33**, 1954 (1997).
 - [33] A. Macchi, *A Superintense Laser-Plasma Interaction Theory Primer*, SpringerBriefs in Physics (Springer Netherlands, Dordrecht, 2013).
 - [34] V. Ritus, *Journal of Russian Laser Research* **6**, 497 (1985).
 - [35] C. P. Ridgers, J. G. Kirk, R. Duclous, T. G. Blackburn, C. S. Brady, K. Bennett, T. D. Arber, and A. R. Bell, *Journal of Computational Physics* **260**, 273 (2014), arXiv:1311.5551.
 - [36] T. Erber, *Reviews of Modern Physics* (1966).
 - [37] V. N. Baier, V. M. Katkov, and V. M. Strakhovenko, *Electromagnetic Processes at High Energies in Oriented Single Crystals* (World Scientific, 1998).
 - [38] J. G. Kirk, a. R. Bell, and I. Arka, *Plasma Physics and Controlled Fusion* **51**, 085008 (2009).
 - [39] B. King and H. Ruhl, *Physical Review D - Particles, Fields, Gravitation and Cosmology* **88**, 1 (2013).
 - [40] V. N. Baier and V. M. Katkov, *Sov. Phys. JETP* **26**, 854 (1968).
 - [41] A. A. Mironov, N. B. Narozhny, and A. M. Fedotov, *Phys. Lett. A* **378**, 3254 (2014).
 - [42] T. D. Arber, K. Bennett, C. S. Brady, A. Lawrence-Douglas, M. G. Ramsay, N. J. Sircombe, P. Gillies, R. G. Evans, H. Schmitz, A. R. Bell, and C. P. Ridgers, *Plasma Physics and Controlled Fusion* **57**, 113001 (2015).
 - [43] S. Gordienko and a. Pukhov, *Physics of Plasmas* **12**, 1 (2005), arXiv:0410268 [physics].
 - [44] A. Kemp, F. Fiuza, A. Debayle, T. Johzaki, W. Mori, P. Patel, Y. Sentoku, and L. Silva, *Nuclear Fusion* **54**, 054002 (2014).
 - [45] A. Robinson, D. Strozzi, J. Davies, L. Gremillet, J. Honrubia, T. Johzaki, R. Kingham, M. Sherlock, and A. Solodov, *Nuclear Fusion* **54**, 054003 (2014).
 - [46] H. Chen, F. Fiuza, a. Link, a. Hazi, M. Hill, D. Hoarty, S. James, S. Kerr, D. Meyerhofer, J. Myatt, J. Park, Y. Sentoku, and G. Williams, *Physical Review Letters* **114**, 1 (2015).
 - [47] G. Sarri, K. Poder, J. M. Cole, W. Schumaker, B. Reville, a. D. Piazza, D. Doria, L. Gizzi, G. Grittani, S. Kar, C. H. Keitel, K. Krushelnick, S. Kuschel, S. P. D. Mangles, Z. Najmudin, D. R. Symes, a. G. R. Thomas, M. Vargas, and M. Zepf, *Nature Communications* **6**, 1 (2015).
 - [48] S. Bulanov, *Physics Letters A* **299**, 240 (2002).
 - [49] F. Fiuza, A. Stockem, E. Boella, R. Fonseca, L. Silva, D. Haberberger, S. Tochitsky, C. Gong, W. Mori, and C. Joshi, *Physical Review Letters* **109**, 215001 (2012).
 - [50] A. Giulietti, G. Bussolino, L. Fulgentini, P. Koester, L. Labate, and L. A. Gizzi, in *Progress in Ultrafast Intense Laser Science XII* (Springer, 2015) pp. 151–178.
 - [51] K. W. D. Ledingham, *Science* **300**, 1107 (2003).
 - [52] R. D. Blandford and R. L. Znajek, *Monthly Notices of the Royal Astronomical Society* **179**, 433 (1977).
 - [53] S. V. Bulanov, T. Z. Esirkepov, M. Kando, J. Koga, K. Kondo, and G. Korn, *Plasma Physics Reports* **41**, 1 (2015).
 - [54] V. Baier and V. Katkov, *Sov. Phys. JETP* **26**, 854 (1968).